

Surface analysis via fast atom diffraction: pattern visibility and spot-beam contribution

L. Frisco,¹ J. E. Miraglia,^{2,1} and M. S. Gravielle²

¹*Dpto. de Física, FCEN, Universidad de Buenos Aires, Buenos Aires, Argentina*

²*Instituto de Astronomía y Física del Espacio (IAFE, CONICET-UBA),
casilla de correo 67, sucursal 28, C1428EGA, Buenos Aires, Argentina*

(Dated: September 9, 2021)

Grazing incidence fast atom diffraction (GIFAD or FAD) is a sensitive tool for surface analysis, which strongly relies on the quantum coherence of the incident beam. In this article the influence of the incidence conditions and the projectile mass on the visibility of the FAD patterns is addressed. Both parameters determine the transverse coherence length of the impinging particles, which governs the general features of FAD distributions. We show that by varying the impact energy, while keeping the same collimating setup and normal energy, it is possible to control the interference mechanism that prevails in FAD patterns. Furthermore, we demonstrate that the contribution coming from different positions of the focus point of the incident particles, which gives rise to the spot-beam effect, allows projectiles to explore different zones of a single crystallographic channel when a narrow surface area is coherently lighted. In this case the spot-beam effect gives also rise to a non-coherent background, which contributes to the gradual quantum-classical transition of FAD spectra. Present results are compared with available experimental data, making evident that the inclusion of focusing effects is necessary for the proper theoretical description of the experimental distributions.

PACS numbers: 34.35.+a, 79.20.Rf, 37.25.+k

I. INTRODUCTION

Over the years surface analysis techniques involving collisions with atomic particles have strongly contributed to the characterization of the surface properties of solids. Among them, grazing-incidence fast atom diffraction (GIFAD or FAD), developed in the last decade [1, 2], can be considered as one of the most sensitive methods to investigate the morphological and electronic characteristics of ordered surfaces [3]. FAD is a versatile analysis technique that can be applied to a wide variety of materials [4–11], providing structural parameters of the topmost atomic layer with an extraordinary accuracy [12–17].

Since the use of FAD as a surface analysis tool requires of both the observation of well-resolved interference structures and its appropriate theoretical description, an essential aspect is the degree of quantum coherence of the incident beam, which governs the general shape of FAD patterns. The degree of coherence of the incident particles depends on the collimating setup and the incidence conditions. In Refs. [18–20] it was shown that for a given collision system, with fixed incidence energy and angle, the experimental collimating scheme determines the overall features of the projectile distribution, allowing one to examine two different interference mechanisms - inter-channel or intra-channel interferences - by varying the size of the collimating slit. This behavior is related to the transverse length of the surface area that is coherently lighted by the incident beam, whose knowledge becomes crucial for an appropriate comparison between experiments and simulations.

In an equivalent way, the incidence conditions are expected to affect the interference spectra produced via FAD by using a given collimating setup [21, 22]. In this

article we explore the influence of the energy and mass of the impinging projectile [23], as well as the width of the incidence channel, on the visibility of FAD patterns obtained with a fixed collimating aperture. Furthermore, the contribution of the spot-beam effect, associated with random-distributed focus points of the incident particles, is addressed. We demonstrate that this effect allows projectiles to probe different regions of the atom-surface potential when the transverse coherence length of the impinging atoms is smaller than the width of the channel. But in this case the spot-beam effect gives rise to a non-coherent background, which strongly modifies the visibility of the interference structures, contributing to the transition from quantum to classical projectile distributions.

The study is confined to fast He and Ne atoms grazing impinging on LiF(001) along the $\langle 110 \rangle$ and $\langle 100 \rangle$ channels. In order to derive the extent of the surface region that is coherently illuminated by the atomic beam after collimation we resort to the Van Cittert-Zernike theorem [20, 24]. This information is then used to determine the size of the coherent initial wave packet to be evolved within the Surface-Initial Value Representation (SIVR) approximation [25]. The SIVR approach is a semi-quantum method that has proved to provide a successful description of experimental FAD patterns for different collision systems [19, 26, 27], offering a clear account of the different interference mechanisms. In this version of the SIVR approximation we also include the variation of the relative position of the focus point (wave-packet center) of the incident particles on the crystal surface, which gives rise to the spot-beam effect.

The paper is organized as follows: The theoretical formalism, including the spot-beam contribution, is summa-

ized in Sec. II. Results for different incidence conditions - incidence energy and channel - and projectile masses are presented and discussed in Secs. III.A and III.B, respectively. In Sec. III.C the contribution of the spot-beam effect is analyzed, while in Sec. III.D we study the gradual quantum-classical transition of the projectile distributions. Finally, Sec. III.E our results are contrasted with available experimental data and in Sec. IV we outline our conclusions. Atomic units (a.u.) are used unless otherwise stated.

II. THEORETICAL MODEL

In this work we extend the previous SIVR model [25] to deal with different focus points of the incident particles. The relative position of the focus point of the beam, with respect to the surface lattice sites, plays a negligible role when the transverse coherence length of the impinging particles is longer than or equal to the width of the incidence channel. But it gains importance as the transverse coherence length decreases. Since it is not experimentally possible to control the focus position of the incident projectiles at such an accuracy level, we consider that each atomic projectile impacts on the surface plane at a different position \mathbf{R}_s , which coincides with the central position of the initial coherent wave packet.

For a given position \mathbf{R}_s of the focus point, the SIVR scattering amplitude for the elastic transition $\mathbf{K}_i \rightarrow \mathbf{K}_f$, \mathbf{K}_i (\mathbf{K}_f) being the initial (final) momentum of the atomic projectile, with $|\mathbf{K}_f| = |\mathbf{K}_i|$, can be expressed as [25]

$$A_{if}^{(SIVR)}(\mathbf{R}_s) = \int d\mathbf{r}_o f_i(\mathbf{r}_o - \mathbf{R}_s) \times \int d\mathbf{k}_o g_i(\mathbf{k}_o) a_{if}^{(SIVR)}(\mathbf{r}_o, \mathbf{k}_o), \quad (1)$$

where $a_{if}^{(SIVR)}(\mathbf{r}_o, \mathbf{k}_o)$ is the partial transition amplitude, given by Eq. (9) of Ref. [25], which is associated with the classical projectile path $\mathbf{r}_t \equiv \mathbf{r}_t(\mathbf{r}_o, \mathbf{k}_o)$, with \mathbf{r}_o and \mathbf{k}_o being the starting position and momentum, respectively, at the time $t = 0$. In Eq. (1) functions $f_i(\mathbf{r}_o - \mathbf{R}_s)$ and $g_i(\mathbf{k}_o)$ describe the spatial and momentum profiles of the initial coherent wave packet at a fixed distance z_o from the surface where the atomic projectile is hardly affected by the surface interaction. The frame of reference is located on the first atomic layer, with the \hat{x} versor along the incidence channel and the \hat{z} versor oriented perpendicular to the surface, aiming towards the vacuum region (see Fig. 1). Within this reference frame, the starting position at $t = 0$ can be expressed as $\mathbf{r}_o = \mathbf{r}'_o + z_o\hat{z}$, where $\mathbf{r}'_o = x_o\hat{x} + y_o\hat{y}$ is the component parallel to the surface plane and the normal distance z_o is chosen as equal to the lattice constant.

To derive the spatial profile of the initial wave packet we assume that the atomic beam is produced by an extended incoherent quasi-monochromatic source, placed at a long distance from a rectangular collimating aperture,

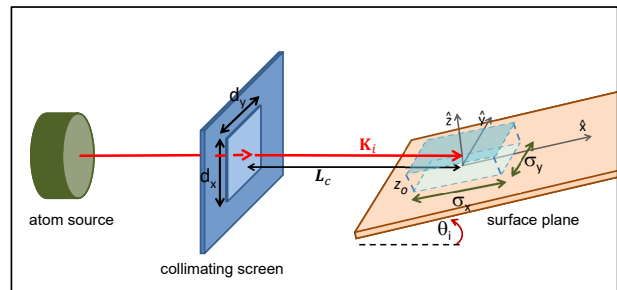


FIG. 1: Depiction of the collimating scheme, together with the reference frame.

with sides d_x and d_y . The collimating slit is oriented perpendicular to the momentum \mathbf{K}_i , in such a way that the side of length d_y is parallel to the surface (i.e. parallel to the \hat{y} versor), while the side of length d_x forms an angle $\theta_x = \pi/2 - \theta_i$ with the surface plane (i.e. with the \hat{x} versor), with θ_i being the glancing incidence angle, as depicted in Fig. 1. The function $f_i(\mathbf{r}'_o - \mathbf{R}_s)$ is here obtained from the complex degree of coherence by applying the Van Cittert-Zernike theorem [24], as explained in Refs. [19, 20]. Under the condition of extended source, given by Eqs. (A.9) and (A.10) of Ref. [20], it can be approximate by means of normalized Gaussian functions $G[\omega, x] = [2/(\pi\omega^2)]^{1/4} \exp(-x^2/\omega^2)$, as

$$f_i(\mathbf{r}'_o - \mathbf{R}_s) \simeq G[\sigma_x, x_o - X_s] G[\sigma_y, y_o - Y_s], \quad (2)$$

where

$$\sigma_x = \frac{L_c \lambda_\perp}{\sqrt{2} d_x}, \quad \sigma_y = \frac{L_c \lambda}{\sqrt{2} d_y}, \quad (3)$$

denote the *transverse coherence lengths* of the initial coherent wave packet [28] along the \hat{x} - and \hat{y} - directions, respectively, and the two-dimensional vector $\mathbf{R}_s = X_s\hat{x} + Y_s\hat{y}$ corresponds to the central position of the wave packet. In Eq. (3), L_c is the collimator-surface distance, $\lambda = 2\pi/K_i$ is the de Broglie wavelength of the impinging atom, and $\lambda_\perp = \lambda/\sin\theta_i$ is the perpendicular wavelength associated with the initial motion normal to the surface plane. The momentum profile $g_i(\mathbf{k}_o)$ is derived from Eq. (2) by applying the Heisenberg uncertainty relation, reading [19, 20]

$$g_i(\mathbf{k}_o) \simeq g_i(\Omega_o) = G(\omega_\theta, \theta_o - \theta_i) G(\omega_\varphi, \varphi_o), \quad (4)$$

where $\Omega_o \equiv (\theta_o, \varphi_o)$ is the solid angle associated with the \mathbf{k}_o - direction, $k_o = K_i$, and

$$\omega_\theta = \frac{d_x}{\sqrt{2} L_c}, \quad \omega_\varphi = \frac{d_y}{\sqrt{2} L_c}. \quad (5)$$

Taking into account that FAD patterns are essentially produced by the interference of a single projectile with itself, contributions to the scattering probability coming from different focus points of the impinging particles must be added incoherently. Thence, the differential scattering probability in the direction of the solid angle Ω_f can be obtained from Eq. (1), except for a normalization factor, as

$$\frac{dP^{(SIVR)}}{d\Omega_f} = \int d\mathbf{R}_s \left| A_{if}^{(SIVR)}(\mathbf{R}_s) \right|^2, \quad (6)$$

where $\Omega_f \equiv (\theta_f, \varphi_f)$ is the solid angle corresponding to the \mathbf{K}_f - direction, with θ_f the final polar angle, measured with respect to the surface, and φ_f the azimuthal angle, measured with respect to the \hat{x} axis. In Eq. (6), the \mathbf{R}_s - integral involves different relative positions within the crystal lattice, covering an area equal to a reduced unit cell of the surface.

III. RESULTS

To study the effect of the coherence length on FAD patterns, in Ref. [19] the size of the collimating aperture was varied by maintaining a fixed incidence condition, i.e., 1 keV He atoms impinging on a LiF(001) surface along $\langle 110 \rangle$ with $\theta_i = 0.99$ deg, in order to compare with the available experiments [18]. The goal of this work is to extend such research by analyzing the influence of the impact energy, the incidence channel and the projectile mass [23], as well as the contribution of the spot-beam effect, for a given collimating setup. For this purpose we examine final angular distributions of ^4He and ^{20}Ne atoms elastically scattered from LiF(001) along the $\langle 110 \rangle$ and $\langle 100 \rangle$ channels, after passing through a square collimating aperture with $d_x = d_y = 0.2$ mm, situated at a distance $L_c = 25$ cm from the surface plane [18]. For both projectiles the surface-atom interaction was evaluated with an improved pairwise additive potential [29], which includes non-local terms of the electronic density in the kinetic, exchange and correlation energies. The potential model also takes into account projectile polarization and rumpling effects. In turn, for the numerical evaluation of the SIVR transition probability we employed the MonteCarlo technique to solve the six-dimensional integral involved in Eqs. (1) and (6), i.e., on $\mathbf{r}'_o \equiv (x_o, y_o)$, $\Omega_o \equiv (\theta_o, \varphi_o)$, and $\mathbf{R}_s \equiv (X_s, Y_s)$, using about 10^7 points. Each of these points involves a further time integration along the classical path, included in $a_{if}^{(SIVR)}(\mathbf{r}_o, \mathbf{k}_o)$, which was evaluated with a step-adaptive integration method [25].

A. Influence of the incidence conditions

We start studying the dependence of the general features of the FAD patterns on the total energy E , with

$E = K_i^2/(2m_P)$ and m_P being the projectile mass. Due to the fast velocity of the projectile along the incidence channel, which makes its parallel motion mainly sensitive to the average potential in this direction, FAD patterns from LiF surfaces are essentially governed by the normal energy $E_\perp = E \sin^2 \theta_i$, which is associated with the slow motion of the atom in the perpendicular plane [3]. Along this article, except in Sec. III. E, we have kept the normal energy $E_\perp = 0.3$ eV as a constant for the different impact energies.

In Fig. 2 we show $dP^{(SIVR)}/d\Omega_f$, as a function of θ_f and φ_f , for He projectiles scattered along the (a) $\langle 110 \rangle$ and (b) $\langle 100 \rangle$ directions with different impact energies, ranging from 0.8 to 8 keV. Since neither inelastic processes nor the detector resolution function were taken into account in the present SIVR calculations, for a given channel and E_\perp - value, all the angular distributions are expected to display the same number of interference maxima, independently of the total impact energy [30]. However, in Fig. 2 this behavior is verified for incidence along $\langle 100 \rangle$ only, while on the contrary, the distributions corresponding to the $\langle 110 \rangle$ direction display interference peaks whose number and relative intensities depend strongly on E . This unexpected fact can be understood in terms of the number of equivalent parallel channels that are coherently illuminated by the atomic beam, as it will be discussed below.

It is now well-established that the structures of FAD spectra come from the combination of inter- and intra-channel interferences [3]. Each of these mechanisms is associated with a different factor of the SIVR transition amplitude [25]: The inter-channel factor, produced by interference among equivalent trajectories running along different parallel channels, which gives rise to equally spaced and intense Bragg peaks, and the intra-channel factor, due to interference inside a single channel, which originates supernumerary rainbow maxima [3, 31]. Accordingly, when the surface area coherently lighted by the atomic beam covers a region containing an array of parallel channels, FAD patterns display Bragg peaks whose intensities are modulated by the intra-channel factor. But when only one channel is coherently illuminated, the spectra present supernumerary rainbow peaks, without any trace of Bragg interference. Thence, the number N of coherently lighted channels results a critical parameter that determines the general shape of FAD distributions. It can be roughly estimated from the transverse coherence length of the incident particles as

$$N \simeq \frac{2\sigma_y}{a_y} = \frac{\sqrt{2}L_c}{d_y} \frac{2\pi}{a_y K_i}, \quad (7)$$

where σ_y is given by Eq. (3) and a_y denotes the width of the incidence channel, with $a_y = 5.4$ a.u. ($a_y = 3.8$ a.u.) for $\langle 110 \rangle$ ($\langle 100 \rangle$).

For a given collimating setup, the value of N varies with both the impact energy, through its dependence on K_i , and the incidence direction, through the channel width, as given by Eq. (7). In Fig. 2 (a), corresponding

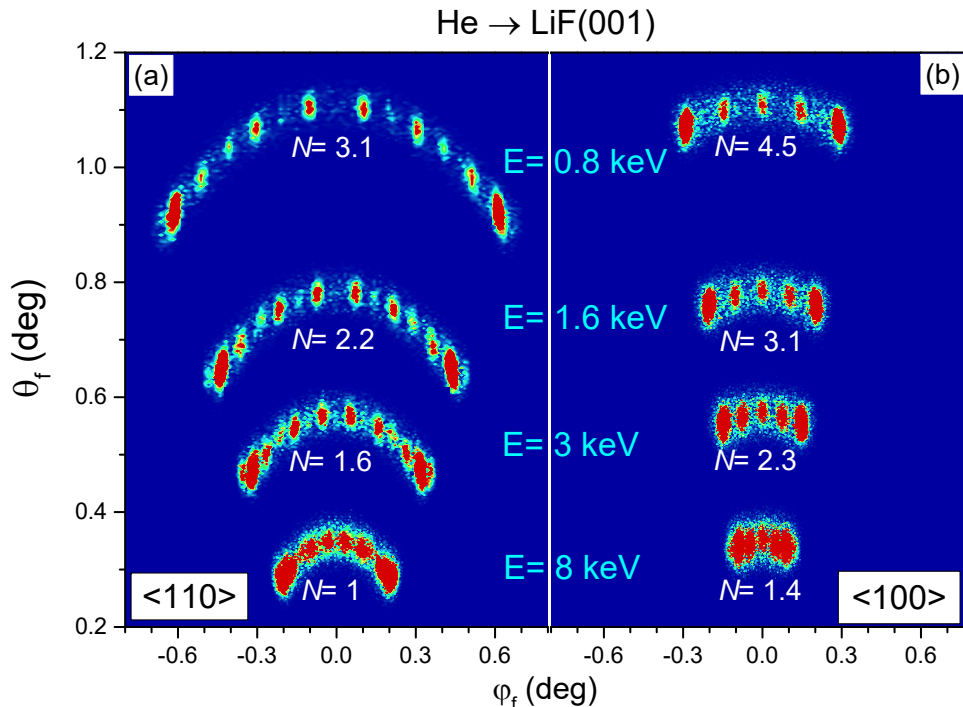


FIG. 2: (Color online) Two-dimensional projectile distributions, as a function of θ_f and φ_f , for He atoms impinging on LiF(001) along the (a) $\langle 110 \rangle$ and (b) $\langle 100 \rangle$ directions. The helium beam is collimated by means of a square aperture of sides $d_x = d_y = 0.2$ mm and the normal energy is $E_{\perp} = 0.3$ eV. In both panels, angular distributions for different impact energies - $E = 0.8, 1.6, 3,$ and 8 keV - are shown, indicating the corresponding N values, as given by Eq. (7).

to the $\langle 110 \rangle$ direction, the application of Eq. (7) for the lowest energy - $E = 0.8$ keV - leads to $N = 3.1$ parallel channels coherently lighted by the He beam, which gives rise to a projectile distribution with well separated Bragg peaks [30]. But when E augments, and consequently, N decreases, these Bragg maxima broaden [25], causing the interference structures for $E = 1.6$ keV to become comparatively wider than those for $E = 0.8$ keV. In Fig. 2 (a) the Bragg peaks for $\langle 110 \rangle$ incidence start to blur out for a total energy about 3 keV, for which $N = 1.6$, while the limit case corresponding to *pure* intra-channel interference is reached at $E = 8$ keV. At this energy a single $\langle 110 \rangle$ channel is coherently illuminated by the incident beam, producing a projectile distribution with rainbow and supernumerary rainbow maxima only. In contrast with this strong dependence on E of the $\langle 110 \rangle$ patterns, in Fig. 2 (b), for the same impact energies but along $\langle 100 \rangle$ all the spectra display a constant number of Bragg peaks (i.e., 5 peaks), in accord with N values higher than 1, varying from $N = 4.5$ to 1.4 for the lowest and highest energies, respectively.

In order to investigate thoroughly the energy dependence of the projectile distributions displayed in Fig. 2 (a), in Fig. 3 we plot the corresponding SIVR differential probabilities as a function of the deflection angle $\Theta = \arctan(\varphi_f / \theta_f)$. Under ideal scattering condi-

tions, involving the incidence of transversely extended wave packets, these Θ - distributions are expected to be independent of E at the same E_{\perp} [30, 32]. Nevertheless, in concordance with Fig. 2 (a), we remarkably found that the spectra of Fig. 3 are severely affected by the total energy if the same collimating setup is used in all the cases. For $E = 0.8$ keV [$N = 3.1$] the projectile distribution as a function of the deflection angle displays well defined Bragg peaks, placed at the angular positions Θ_m (indicated with vertical dashed lines in Fig. 3) satisfying $\sin \Theta_m = m\lambda_{\perp}/a_y$, where $m = 0, \pm 1, \pm 2, \dots$ denotes the Bragg order. But since the width of the Bragg peaks depends on N [25], these Bragg structures fade out progressively as the energy increases, bringing into light supernumerary rainbows, as observed for $E = 8$ keV at the top of Fig. 3. In addition, all the spectra of Fig. 3 display high-intensity rainbow maxima at the outermost angles, which have a classical origin [33].

B. Influence of the projectile mass

The angular distributions of neon atoms scattered along the $\langle 110 \rangle$ channel, plotted in Fig. 4, display a behavior analogous to that shown in Fig. 3 for helium. However, for Ne projectiles the dependence of N on the

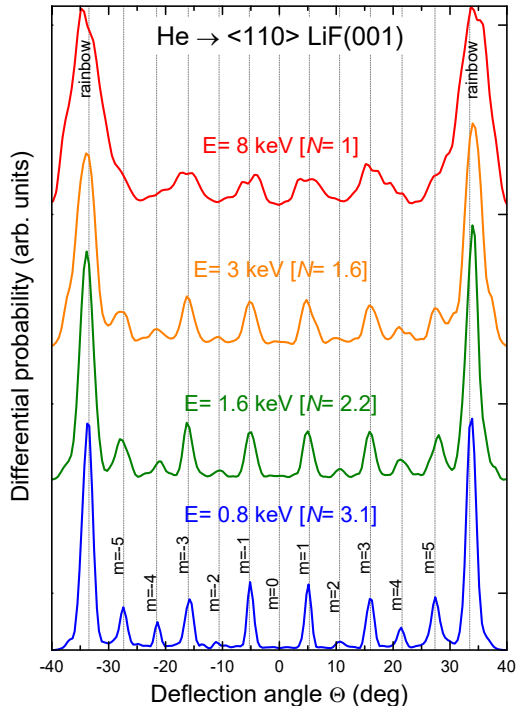


FIG. 3: (Color online) Angular spectra, as a function of the deflection angle Θ , for the cases considered in Fig. 2 (a). Dashed vertical lines, Θ_m - positions of Bragg peaks.

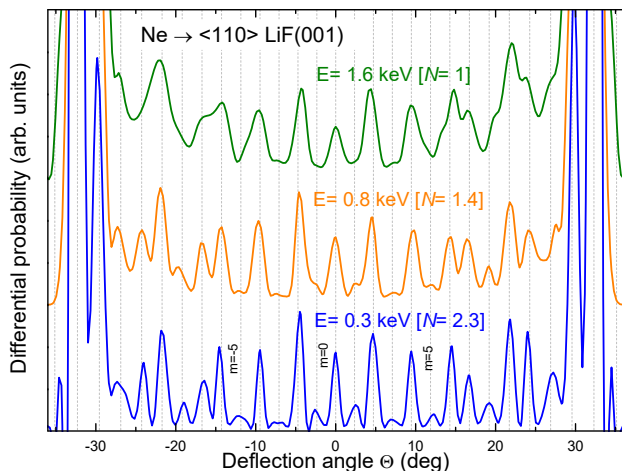


FIG. 4: (Color online) Analogous to Fig. 3 for Ne atoms impinging on LiF(001) along the $\langle 110 \rangle$ direction, with $E_{\perp} = 0.3$ eV.

atomic mass, through the initial momentum as given by Eq. (7), originates a reduction of the number of coherently lighted channels in comparison with He at the same impact energy. Therefore, under the same collimating conditions the limit energy for the observation of inter-channel interference in Ne spectra results to be about 5 times lower than in the case of He impact. Hence, in Fig.

4 the Ne distribution for $E = 1.6$ keV shows only supernumerary rainbow maxima, which contrasts with the Bragg structures of Fig. 3 for the same impact energy of He projectiles. Notice that in Fig. 4 well-resolved Bragg peaks are only present in the Ne distribution for $E = 0.3$ keV [$N = 2.3$], which is comparable to that for 1.6 keV He projectiles in Fig. 3. These results suggest that the transverse coherence length might be the central parameter that limits the observation of Bragg peaks in experimental Ne spectra, rather than the thermal vibrations of the surface atoms or the spatial resolution of the detector, as it was previously considered [34].

C. Contribution of the spot-beam effect

All the results presented in the previous Sections were obtained from coherently illuminated regions with a transverse length longer than or equal to the channel width, that is, with $N \gtrsim 1$. Under such a constraint, the SIVR transition amplitudes corresponding to different focus points of the beam, given by Eq. (1), are alike, leading to

$$dP^{(SIVR)}/d\Omega_f \simeq \left| A_{if}^{(SIVR)}(\mathbf{R}_s = 0) \right|^2, \quad (8)$$

where $\mathbf{R}_s = 0$ indicates a focus point situated just in the middle of the incidence channel, here named central focus point.

But when the impact energy augments beyond the limit of *pure* intra-channel interference, and consequently, the coherently lighted area shrinks, covering a surface region narrower than a_y , the different Y_s coordinates of the focus points give rise to dissimilar partial projectile distributions $\left| A_{if}^{(SIVR)}(\mathbf{R}_s) \right|^2$. Each of these partial distributions probes a different zone of the atom-surface potential within the channel, causing the contribution of the spot-beam effect, associated with the \mathbf{R}_s -integral in Eq. (6), to become important.

In order to study the energy dependence of the spot-beam effect, in Fig. 5 we show $dP^{(SIVR)}/d\Theta$, as a function of the deflection angle, for Ne atoms impinging along the $\langle 110 \rangle$ channel with total energies (a) $E = 2$, (b) 3, and (c) 8 keV, which correspond to $N = 0.9$, 0.7, and 0.4, respectively. In all the panels, results derived from Eq. (6), including the spot-beam contribution, are contrasted with those obtained by considering only *pure* intra-channel interference, as given by Eq. (8) for $N = 1$. From Fig. 5 we found that the spot-beam contribution keeps the angular positions of supernumerary maxima, but introduces a non-coherent background in the central region of the spectrum, around the direction of specular reflection (i.e., $\Theta \simeq 0$), in relation to that for single-channel illumination. The angular extension of such a spot-beam background is sensitive to N , increasing as N diminishes, as observed by comparing Figs. 5 (a) and (b).

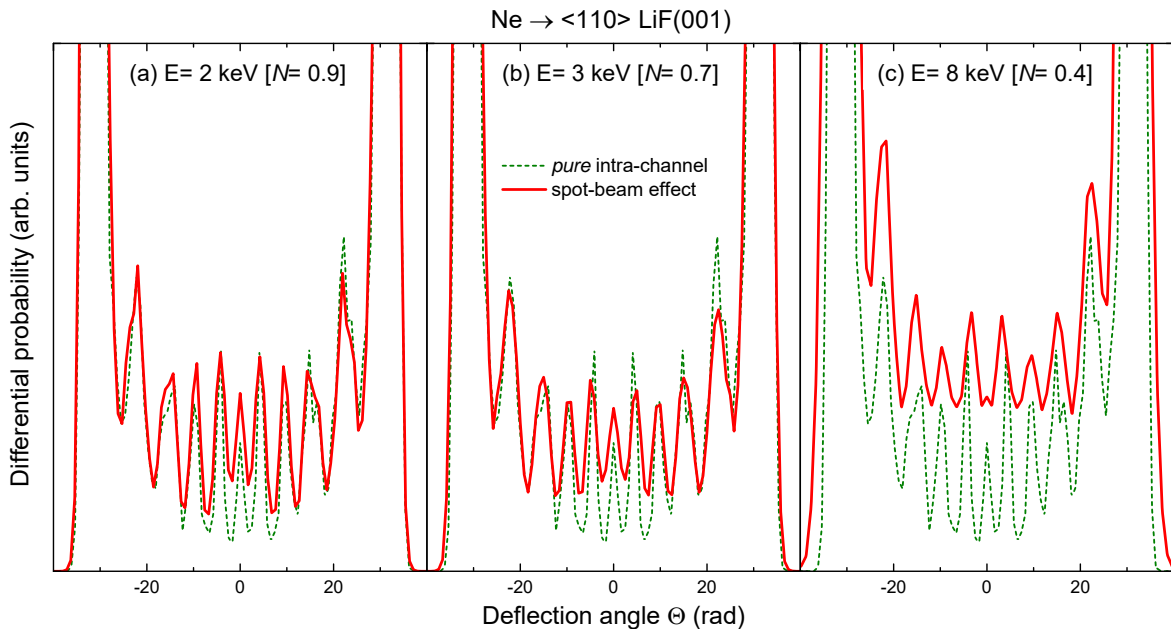


FIG. 5: (Color online) Angular spectra, as a function of the deflection angle Θ , for Ne atoms along the $\langle 110 \rangle$ direction, with $E_{\perp} = 0.3$ eV. Results for (a) $E = 2$ keV [$N = 0.9$], (b) $E = 3$ keV [$N = 0.7$], and (c) $E = 8$ keV [$N = 0.4$] are displayed. Red solid line, angular distribution including the spot-beam effect, as given by Eq. (6); dark-green dashed line, *pure* intra-channel distribution corresponding to $N = 1$, given by Eq. (8).

The role played by the spot-beam effect is even more relevant when the transverse length of the surface area that is coherently illuminated by the beam is about or smaller than the half width of the incidence channel. In Fig. 5 (c) the projectile distribution for 8 keV Ne atoms (i.e., $N = 0.4$) is severely affected by the spot-beam effect when it is contrasted with that corresponding to $N = 1$. Different \mathbf{R}_s positions allow projectiles to separately explore zones of the potential energy surface with positive or negative slope, producing interference structures placed at negative or positive deflection angles, respectively. Only when these partial contributions are added, as given by Eq. (6), the angular spectrum including the spot-beam contribution presents defined supernumerary peaks in the whole angular range. But in this case the spot-beam effect gives also rise to a wide non-coherent background, which reduces the visibility of the interference patterns, in comparison with that of the *pure* intra-channel spectrum, as it will be discussed in the next Section.

D. Focusing effect in the transition from quantum to classical distributions

In this Section we investigate how the decreasing of N below the unit reduces the visibility of the diffraction patterns, leading to the gradual switch from quantum projectile distributions, containing intra-channel interference structures, to classical spectra without signatures

of interference. With this aim it is convenient to analyze the profile of the atom-surface potential near the reflection region of projectiles, which governs the intra-channel interference in a first approach. Beforehand, we stress that our SIVR calculations were obtained from a three-dimensional atom-surface potential and no dimension reduction was made during the dynamics. However, since FAD patterns are essentially sensitive to the averaged potential energy surfaces along the incidence channel, such effective equipotential contours provide useful insights of the intra-channel interference mechanism.

For Ne atoms impinging on LiF(001) along the $\langle 110 \rangle$ direction, in Fig. 6 (a) we plot the averaged equipotential curve $-z(y)$ - corresponding to $E_{\perp} = 0.3$ eV, as a function of the coordinate y across the channel, normalized by the width a_y . Within this simplified picture, the intra-channel interference is produced by the coherent addition of transition amplitudes $a_{if}^{(SIVR)}(\mathbf{r}_o, \mathbf{k}_o)$ corresponding to trajectories reflecting at turning points with different y coordinates inside the channel, but with the same slope dz/dy of the averaged equipotential curve, which determines the final azimuthal angle [3]. For the present case, from Fig. 6 (b) it is observed that there are only two different trajectories that contribute to the intra-channel interference pattern at a given angular position φ_f , except around rainbow angles where several (infinite) turning points coalesce at a maximum or minimum of dz/dy . Then, in FAD distributions an essential requirement to observe a supernumerary rainbow structure at a given φ_f or Θ angle (inside the angular range

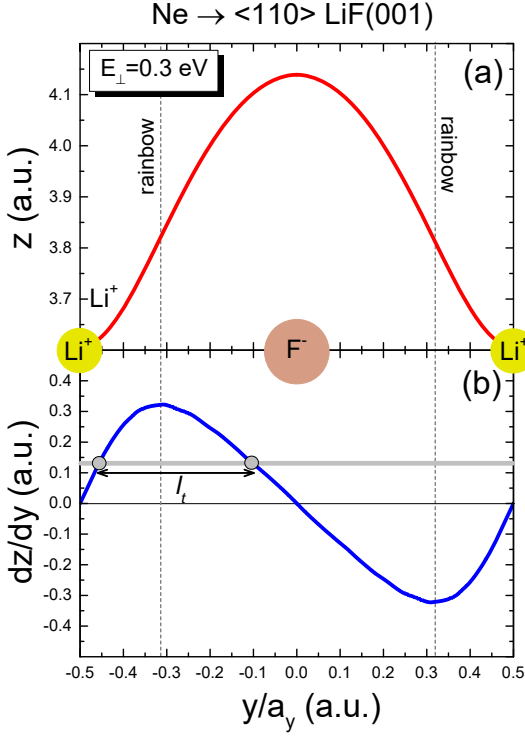


FIG. 6: (Color online) Analysis of the equipotential contour, averaged along the $\langle 110 \rangle$ channel, for the Ne-LiF(001) interaction. (a) Red solid line, equipotential curve $z(y)$ for $E_{\perp} = 0.3$ eV; (b) derivative dz/dy of the equipotential curve of (a). Gray circles, turning point positions corresponding to two different trajectories that interfere at a given deflection angle; vertical dashed lines indicate turning point positions corresponding to trajectories that contribute to the rainbow maxima.

defined by the rainbow peaks) is given by the condition that the N value must be longer than $l_t = l_y/a_y$, where l_y denotes the transverse distance between the turning points of the corresponding interfering trajectories. This fact is illustrated in Fig. 7, where the distribution for $N = 0.3$, is displayed. In this case the spectrum obtained including the spot-beam effect does not show the central interference maximum, associated with the highest l_t value (i.e., $l_t = 0.5$ corresponding to two trajectories on top of the Li^+ - and F^- - crystallographic rows, respectively), and supernumerary rainbow peaks are visible at larger deflection angles only. In addition, the visibility of the interference structures diminishes and the spectrum tends to the classical distribution, which displays only pronounced rainbow maxima.

The quantum-classical transition of FAD distributions can be quantitatively studied by analyzing the visibility $\mathcal{V}(n)$ associated with the supernumerary rainbow maximum labelled with n in Fig. 7, where $n = 0, \pm 1, \pm 2, \dots$, $n = 0$ corresponding to the central peak [36]. Like in optics [24], we define the visibility in FAD as

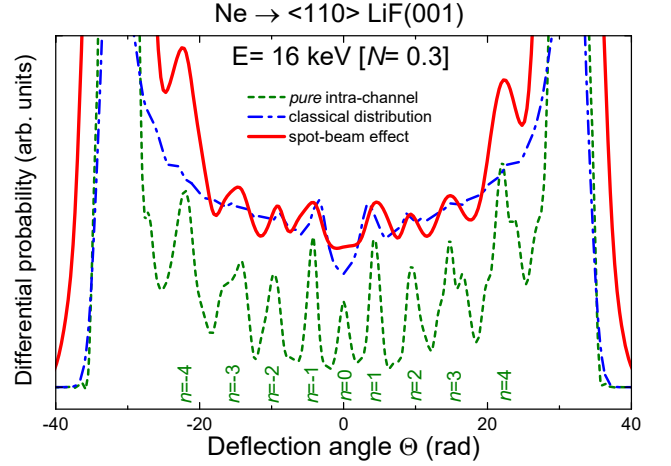


FIG. 7: (Color online) Analogous to Fig. 5 for $E = 16$ keV [$N = 0.3$]. Blue dot-dashed line, classical projectile distribution for $N = 1$. The n values indicate different supernumerary rainbow peaks.

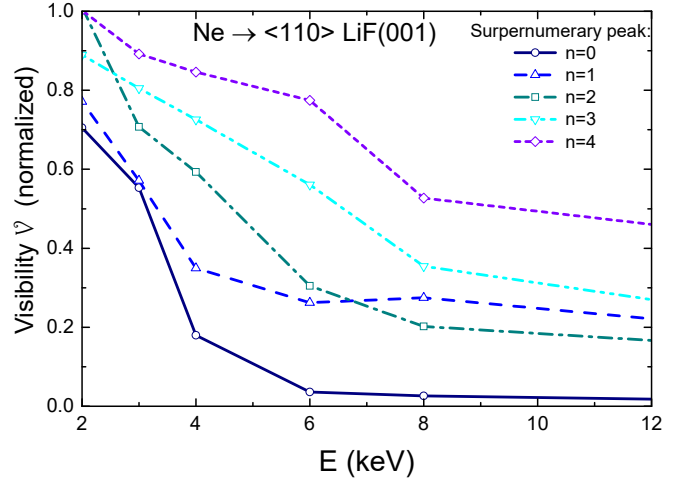


FIG. 8: (Color online) Visibility $\mathcal{V}(n)$ (normalized to that for $N = 1$), as a function of E , for Ne projectiles colliding along $\langle 110 \rangle$ with $E_{\perp} = 0.3$ eV.

$$\mathcal{V}(n) = \frac{I_{\max}^{(n)} - I_{\min}^{(n)}}{I_{\max}^{(n)} + I_{\min}^{(n)}}, \quad (9)$$

where $I_{\max}^{(n)}$ is the differential probability $dP^{(SIVR)}/d\Theta$, derived from Eq. (6), at the n -supernumerary rainbow maximum, and $I_{\min}^{(n)}$ denotes the averaged value of the differential probability at the positions of the two adjacent minima. This visibility provides a measure of the degree of coherence of the atomic beam [24, 37]. In Fig. 8 we show $\mathcal{V}(n)$, normalized to that for $N = 1$, as a function of the impact energy, for Ne projectiles colliding along $\langle 110 \rangle$ with $E_{\perp} = 0.3$ eV. As a consequence of the spot-beam effect, under the same collimating conditions the visibility

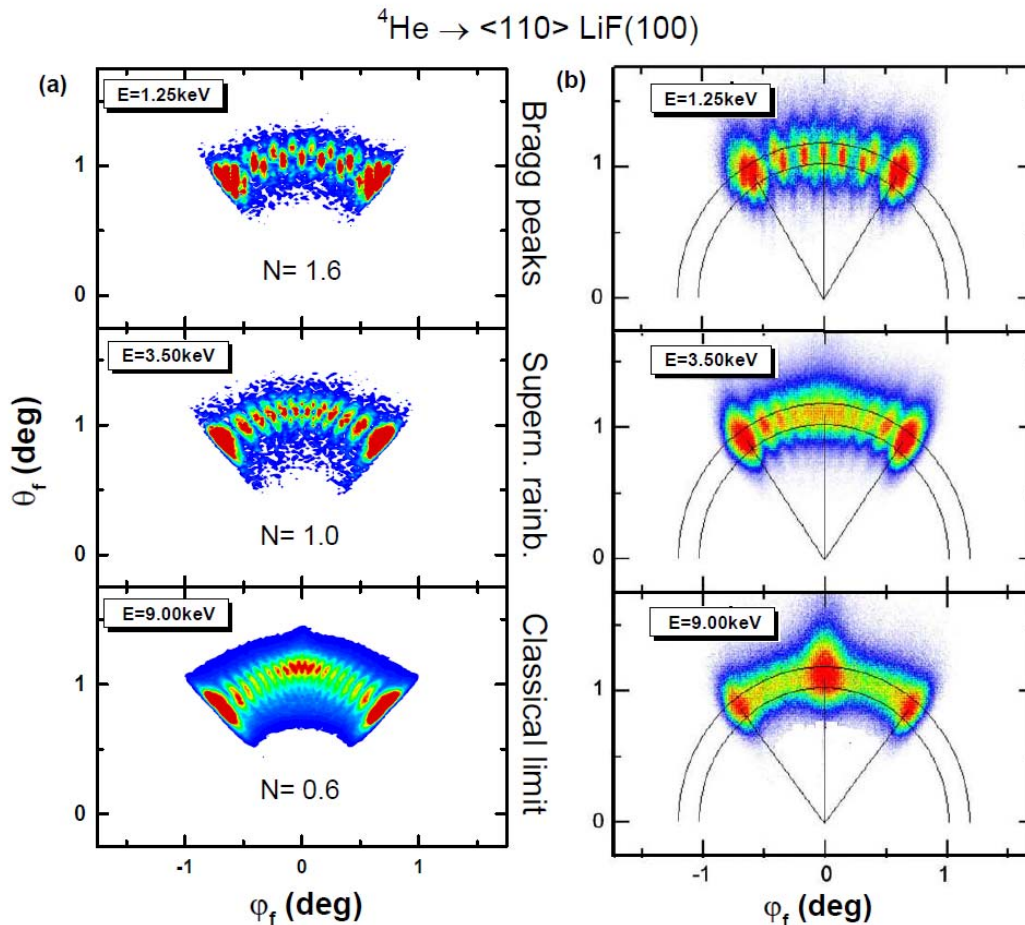


FIG. 9: (Color online) Two-dimensional angular distributions, as a function of θ_f and φ_f , for He atoms impinging on LiF(001) along $\langle 110 \rangle$ with $\theta_i = 1.1$ deg. (a) (right panels) Simulated SIVR results derived by considering a collimating slit of width $d_y = 0.3$ mm. (b) (left panels) Experimental distributions extracted from Ref. [35]. In both columns, different impact energies - $E = 1.25, 3.50,$ and 9.00 keV - are considered. The corresponding N values, as given by Eq. (7), are indicated.

tends to decrease when the energy increases beyond the energy limit of *pure* intra-channel interference. Such a decreasing is more steeply for the central peaks than for the outermost ones, in accord with the condition $N \gtrsim l_t$ for the observation of supernumerary maxima. For higher E (lower N) values, the interference structures gradually blur out and all $\mathcal{V}(n)$ slowly decrease, making projectile distributions reach the classical limit.

E. Experimental comparison

To test the predicted influence of the incidence conditions, in Fig. 9 SIVR simulations derived from Eq. (6) are compared with available experimental distributions [35] for helium atoms impinging on LiF(001) along the $\langle 110 \rangle$ channel. These two-dimensional angular distributions were obtained by varying the impact energy but keeping fixed the incidence angle, i.e., $\theta_i = 1.1$ deg [35]. In order to reproduce the experiments, in this Section

we have considered a rectangular slit with sides $d_x = 1.5$ mm and $d_y = 0.3$ mm, which produces an angular dispersion $\omega_\varphi = 0.05$ deg, comparable to the experimental value [35].

In Fig. 9, for $E = 1.25$ keV (top panels) the theoretical distribution is in accord with the experimental one, showing not fully resolved Bragg peaks associated with $N = 1.6$. Instead, for $E = 3.50$ keV (middle panels) the Bragg peaks completely disappear and the simulated and experimental FAD patterns display only supernumerary maxima corresponding to a single-channel illumination, i.e., to $N = 1$. Lastly, for $E = 9.00$ keV [$N = 0.6$] (lower panels) the interference maxima are barely visible as isolated peaks in the simulated angular spectrum due to the contribution of the spot-beam effect. In this case, both the theoretical and the experimental distributions tend to the classical one, showing a broad high intensity contribution at $\varphi_f = 0$ and two intense rainbow peaks at the outermost angles.

Therefore, the reasonable good agreement between

theory and experiment observed in Fig. 9 strongly suggests that the energy dependence of the general features of experimental FAD distributions is mainly produced by the variation of the transverse coherence length, as it was proposed in Ref. [35]. However, at this point it is necessary to mention that there are other effects not included in our model, like inelastic processes [38], which can contribute to deteriorate the coherence, helping to the transition from quantum to classical projectile distributions. In addition, notice that our simulations do not include thermal vibrations of lattice atoms [29] and the results were not convoluted with the detector resolution, both effects which are expected to smooth the theoretical spectra.

IV. CONCLUSIONS

We have investigated the influence of the total energy, the incidence channel, and the projectile mass on the general characteristics of FAD patterns produced by an atomic beam that collides grazingly on a LiF(001) surface, after passing through a fixed collimating setup. We have shown that, even using the same collimating aperture, it is possible to obtain final projectile distributions containing different interference structures by varying the total energy while keeping the normal energy as a constant. This behavior can be explained in terms of the number N of equivalent parallel channels that are coherently illuminated by the atomic beam.

For a given collimating aperture, the decreasing of N as E increases, originates the gradually broadening of Bragg peaks, until they fade completely out for $N = 1$, bringing to light supernumerary rainbow maxima associated with the *pure* intra-channel interference. The energy ranges corresponding to these interference mechanisms also de-

pend on the projectile mass, making *pure* intra-channel interference be reached at a total energy lower for Ne than for He projectiles, as it was experimentally observed [34].

Furthermore, we have demonstrated that the spot-beam effect, produced by the different positions within the crystal lattice of the focus point of the beam, plays an important role when a portion of a single crystallographic channel is coherently lighted by the impinging particles. In the energy range where $0.4 \lesssim N \lesssim 1$ the spot-beam effect helps to recover supernumerary rainbow maxima symmetrically distributed with respect to the specular direction. But the visibility of these structure decreases as N diminishes, causing that for smaller N values the projectile distributions approximate to the classical ones.

In conclusion, the focusing effects have been shown to be essential to properly describe experimental projectile distributions, which is relevant to use FAD spectra as a surface analysis tool. In this regard, notice that the coherence conditions of the incident beam have been recently found to play an important role in atomic collisions involving not only molecules [39] but also atoms [40, 41] as targets. Hence, FAD distributions might represent an almost ideal benchmark to investigate this problem, being a useful guide for coherence studies on other collision systems. Finally, we should mention that even though present results are in agreement with available experiments [35], further experimental research on this issue is desirable.

Acknowledgments

This work was carried out with financial support from CONICET, UBA and ANPCyT of Argentina.

-
- [1] A. Schüller, S. Wethekam, and H. Winter. Diffraction of Fast Atomic Projectiles during Grazing Scattering from a LiF(001) Surface. *Phys. Rev. Lett.*, 98:016103, 2007.
 - [2] P. Rousseau, H. Khemliche, A. G. Borisov, and P. Roncin. Quantum Scattering of Fast Atoms and Molecules on Surfaces. *Phys. Rev. Lett.*, 98:016104, 2007.
 - [3] H. Winter and A. Schüller. Fast atom diffraction during grazing scattering from surfaces. *Prog. Surf. Sci.*, 86:169–221, 2011.
 - [4] M. Debiossac, A. Zugarramurdi, H. Khemliche, P. Roncin, A. G. Borisov, A. Momeni, P. Atkinson, M. Eddrief, F. Finocchi, and V. H. Etgens. Combined experimental and theoretical study of fast atom diffraction on the $\beta_2(2 \times 4)$ reconstructed GaAs(001) surface. *Phys. Rev. B*, 90:155308, 2014.
 - [5] M. Busch, A. Schüller, S. Wethekam, and H. Winter. Fast Atom Diffraction at Metal Surface. *Surf. Sci.*, 603:L23–L26, 2009.
 - [6] C. A. Ríos Rubiano, G. A. Bocan, M. S. Gravielle, N. Bundaleski, H. Khemliche, and P. Roncin. *Ab initio* potential for the He-Ag(110) interaction investigated using grazing-incidence fast-atom diffraction. *Phys. Rev. A*, 87:012903, 2013.
 - [7] H. Winter, J. Seifert, D. Blauth, M. Busch, A. Schüller, and S. Wethekam. Structure of ultrathin oxide layers on metal surfaces from grazing scattering of fast atoms. *Appl. Surf. Sci.*, 256:365–370, 2009.
 - [8] A. Schüller, M. Busch, S. Wethekam, and H. Winter. Fast Atom Diffraction from Superstructures on a Fe(110) Surface. *Phys. Rev. Lett.*, 102:017602, 2009.
 - [9] J. Seifert, M. Busch, E. Meyer, and H. Winter. Surface Structure of Alanine on Cu(110) Studied by Fast Atom Diffraction. *Phys. Rev. Lett.*, 111:137601, 2013.
 - [10] A. Zugarramurdi, M. Debiossac, P. Lunca-Popa, A. J. Mayne, A. Momeni, A. G. Borisov, Z. Mu, P. Roncin, and H. Khemliche. Determination of the geometric corrugation of graphene on SiC(0001) by grazing incidence fast atom diffraction. *Appl. Phys. Lett.*, 106:101902, 2015.
 - [11] A. Momeni, E. M. Staicu Casagrande, A. Dechaux, and H. Khemliche. Ultrafast Crystallization Dynamics at an

- Organic-Inorganic Interface Revealed in Real Time by Grazing Incidence Fast Atom Diffraction. *J. Phys. Chem. Lett.*, 9:908–913, 2018.
- [12] A. Schüller, S. Wethekam, D. Blauth, H. Winter, F. Aigner, N. Simonović, B. Solleder, J. Burgdörfer, and L. Wirtz. Rumpling of LiF(001) surface from fast atom diffraction. *Phys. Rev. A*, 82:062902, 2010.
- [13] A. Schüller, D. Blauth, J. Seifert, M. Busch, H. Winter, K. Gärtner, R. Włodarczyk, J. Sauer, and M. Sierka. Fast atom diffraction during grazing scattering from a MgO(001) surface. *Surf. Sci.*, 606:161–173, 2012.
- [14] J. Seifert and H. Winter. In-situ monitoring of oxygen adsorption at Mo(112) surface via fast atom diffraction. *Surf. Sci.*, 610:L1–L5, 2013.
- [15] J. Seifert and H. Winter. Quantitative structure determination using grazing scattering of fast atoms: Oxygen-induced missing-row reconstruction of Mo(112). *Phys. Rev. B*, 93:205417, 2016.
- [16] M. del Cueto, A. S. Muzas, M. F. Somers, G. J. Kroes, C. Díaz, and F. Martín. Exploring surface landscapes with molecules: rotationally induced diffraction of H₂ on LiF(001) under fast grazing incidence conditions. *Phys. Chem. Chem. Phys.*, 19:16317–16322, 2017.
- [17] M. Debiossac, P. Atkinson, A. Zugarramurdi, M. Eddrief, F. Finocchi, V. H. Etgens, A. Momeni, H. Khemliche, A. G. Borisov, and P. Roncin. Fast atom diffraction inside a molecular beam epitaxy chamber, a rich combination. *Appl. Surf. Sci.*, 391:53–58, 2017.
- [18] J. Seifert, J. Lienemann, A. Schüller, and H. Winter. Studies on coherence and decoherence in Fast Atom Diffraction. *Nucl. Instrum. Methods Phys. Res. B*, 350:99–105, 2015.
- [19] M. S. Gravielle and J. E. Miraglia. Influence of beam collimation on fast-atom diffraction studied via a semi-quantum approach. *Phys. Rev. A*, 92:062709, 2015.
- [20] M. S. Gravielle and J. E. Miraglia. Single- and double-slit collimating effects on fast-atom diffraction spectra. *Nucl. Instrum. Methods Phys. Res. B*, 382:42–48, 2016.
- [21] J. M. Moix and E. Pollak. Heavy atom quantum diffraction by scattering from surfaces. *J. Chem. Phys.*, 134:011103, 2011.
- [22] M. Minniti, C. Díaz, J. L. Fernández Cuñado, A. Politano, D. Maccariello, F. Martín, D. Farías, and R. Miranda. Helium, neon and argon diffraction from Ru(0001). *J. Phys.: Condens. Matter*, 24:354002, 2012.
- [23] M. S. Gravielle. Fast interaction of atoms with crystal surfaces: coherent lighting. *J. Phys. Conf. Ser.*, 875:012006, 2017.
- [24] M. Born and E. Wolf. *Principles of Optics*, chapter 10. Pergamon Press, Oxford, 1986.
- [25] M. S. Gravielle and J. E. Miraglia. Semiquantum approach for fast atom diffraction: Solving the rainbow divergence. *Phys. Rev. A*, 90:052718, 2014.
- [26] G. A. Bocan, J. D. Fuhr, and M. S. Gravielle. van der Waals effects on grazing-incidence fast-atom diffraction for H on LiF(001). *Phys. Rev. A*, 94:022711, 2016.
- [27] G. A. Bocan and M. S. Gravielle. GIFAD for He/KCl(001). Structure in the pattern for (110) incidence as a measure of the projectile-cation interaction. *Nucl. Instr. Methods Phys. Res. B*, 421:1–6, 2018.
- [28] A. Tonomura. Electron Holography. *Progress in Optics*, 23:183–220, 1986.
- [29] J. E. Miraglia and M. S. Gravielle. Reexamination of the interaction of atoms with a LiF(001) surface. *Phys. Rev. A*, 95:022710, 2017.
- [30] A. Schüller, H. Winter, M. S. Gravielle, J. M. Pruneda, and J. E. Miraglia. He-LiF surface interaction potential from fast atom diffraction. *Phys. Rev. A*, 80:062903, 2009.
- [31] A. Schüller and H. Winter. Supernumerary Rainbows in the Angular Distribution of Scattered Projectiles for Grazing Collisions of Fast Atoms with a LiF(001) Surface. *Phys. Rev. Lett.*, 100:097602, 2008.
- [32] M. S. Gravielle. Quantum interference of fast atoms scattered off crystal surfaces. *J. Phys. Conf. Ser.*, 583:012027, 2015.
- [33] R. Guantes, A. S. Sanz, J. Margalef-Roig, and S. Miret-Artés. Atom-surface diffraction: a trajectory description. *Surf. Sci. Rep.*, 53:199–330, 2004.
- [34] M. S. Gravielle, A. Schüller, H. Winter, and J. E. Miraglia. Fast atom diffraction for grazing scattering of Ne atoms from a LiF(001) surface. *Nucl. Instr. Methods Phys. Res. B*, 269:1208–1211, 2011.
- [35] A. Schüller and H. Winter. Diffraction of fast atoms under axial surface channeling conditions. *Nucl. Instr. Methods Phys. Res. B*, 267:628–633, 2009.
- [36] Notice that the parameter n used to label the different supernumerary maxima does not coincide with the supernumerary rainbow order as defined in ref. [3].
- [37] C. S. Adams, M. Sigel, and J. Mlynek. Atom optics. *Phys. Rep.*, 240:143–210, 1994.
- [38] P. Roncin and M. Debiossac. Elastic and inelastic diffraction of fast atoms, Debye-Waller factor, and Mössbauer-Lamb-Dicke regime. *Phys. Rev. B*, 96:035415, 2017.
- [39] K. N. Egodapitiya, S. Sharma, A. Hasan, A. C. Laforge, D. H. Madison, R. Moshhammer, and M. Schulz. Manipulating Atomic Fragmentation Processes by Controlling the Projectile Coherence. *Phys. Rev. Lett.*, 106:153202, 2011.
- [40] H. Gassert, O. Chuluunbaatar, M. Waitz, F. Trinter, H.-K. Kim, T. Bauer, A. Laucke, Ch. Müller, J. Voigtsberger, M. Weller, J. Rist, M. Pitzer, S. Zeller, T. Jahnke, L. Ph. H. Schmidt, J. B. Williams, S. A. Zaytsev, A. A. Bulychiev, K. A. Kouzakov, H. Schmidt-Böcking, R. Dörner, Yu. V. Popov, , and M. S. Schöffler. Agreement of Experiment and Theory on the Single Ionization of Helium by Fast Proton Impact. *Phys. Rev. Lett.*, 116:073201, 2016.
- [41] L. Sarkadi, I. Fabre, F. Navarrete, and R. O. Barrachina. Loss of wave-packet coherence in ion-atom collisions. *Phys. Rev. A*, 93:032702, 2016.